Design and performance of a 180~L high-pressure xenon gas TPC as a prototype for a large-scale neutrinoless double-beta decay search

AUTHOR(S):

Ban, S; Hirose, M; Ichikawa, A K; Iwashita, Y; Kikawa, T; Minamino, A; Miuchi, K; ... Tanaka, S; Ueshima, K; Yoshida, M

CITATION:

Ban, S ...[et al]. Design and performance of a 180~L high-pressure xenon gas TPC as a prototype for a large-scale neutrinoless double-beta decay search. Progress of Theoretical and Experimental Physics 2020, 2020(3): 033H01.

ISSUE DATE:

2020-03

URL:

http://hdl.handle.net/2433/259309

PTEP
Prog. Theor. Exp. Phys. **2020**, 033H01 (20 pages)
DOI: 10.1093/ptep/ptaa030

Design and performance of a high-pressure xenon gas TPC as a prototype for a large-scale neutrinoless double-beta decay search

S. Ban[1,*], M. Hirose[1], A. K. Ichikawa[1], Y. Iwashita[2], T. Kikawa[1], A. Minamino[3], K. Miuchi[4], T. Nakadaira[5], Y. Nakajima[6,7], K. D. Nakamura[4], K. Z. Nakamura[1], T. Nakaya[1], S. Obara[1,9], K. Sakashita[5], H. Sekiya[6,7], B. Sugashima[1], S. Tanaka[1], K. Ueshima[8], and M. Yoshida[1]

[1]*Department of Physics, Kyoto University, Kyoto 606-8502, Japan*
[2]*Advanced Research Center for Beam Science, Kyoto University, Kyoto 611-0011, Japan*
[3]*Yokohama National University, Faculty of Engineering, Yokohama 240-8501, Japan*
[4]*Department of Physics, Kobe University, Kobe 657-8501, Japan*
[5]*Institute of Particle and Nuclear Studies, High Energy Accelerator Research Organization (KEK), Tsukuba 305-0801, Japan*
[6]*Kamioka Observatory, Institute for Cosmic Ray Research, the University of Tokyo, Hida 506-1205, Japan*
[7]*Kavli Institute for the Physics and Mathematics of the Universe (WPI), the University of Tokyo, Kashiwa 277-8568, Japan*
[8]*Research Center for Neutrino Science, Tohoku University, Sendai 980-8578, Japan*
[9]*Present address: Frontier Research Institute for Interdisciplinary Sciences, Tohoku University, Sendai, 980-8578, Japan*
*E-mail: bansei0526@scphys.kyoto-u.ac.jp

Received January 10, 2020; Revised February 12, 2020; Accepted February 13, 2020; Published March 23, 2020

A high-pressure xenon gas time projection chamber, with a unique cellular readout structure based on electroluminescence, has been developed for a large-scale neutrinoless double-beta decay search. In order to evaluate the detector performance and validate its design, a 180 L size prototype is being constructed and its commissioning with partial detector has been performed. The obtained energy resolution at 4.0 bar is 1.73 ± 0.07% (FWHM) at 511 keV. The energy resolution at the ^{136}Xe neutrinoless double-beta decay Q-value is estimated to be between 0.79 and 1.52% (FWHM) by extrapolation. Reconstructed event topologies show patterns peculiar to the track endpoint that can be used to distinguish $0\nu\beta\beta$ signals from gamma-ray backgrounds.

Subject Index H20

1. Introduction

Whether the neutrino is of Majorana type or not is a crucial question for particle physics and cosmology. If the answer is "yes", neutrinos may have played a central role in creating the matter–antimatter asymmetric universe via the leptogenesis scenario [1]. Extremely light neutrino masses may also be related to the Majorana nature (seesaw mechanism [2,3]). Currently the most practical method to confirm that neutrinos are Majorana particles is to observe neutrinoless double-beta decay ($0\nu\beta\beta$ decay). The strictest lower limit on the half-life of $0\nu\beta\beta$ decay in ^{136}Xe was obtained by the KamLAND-Zen experiment to be 1.07×10^{26} years (90% CL) [4]. Because its lifetime is expected to be very long, the search for $0\nu\beta\beta$ decay requires a ton-scale target mass, an ultra-low radioactive environment, and powerful background rejection. High energy resolution is especially essential to distinguish $0\nu\beta\beta$ decay from continuous backgrounds such as double-beta decay accompanying emission of neutrinos ($2\nu\beta\beta$ decay). High-pressure xenon gas time projection chambers (TPCs) meet these

requirements [5]. The application of high-pressure xenon gas TPCs for $0\nu\beta\beta$ decay searches is being actively pursued by the NEXT [6] and PandaX-III experiments [7]. The former has demonstrated high energy resolution in a high-pressure xenon gas TPC using electroluminescence (EL) [8–10], and the latter is developing a detector with good tracking capabilities using MicroMegas [11].

We are also developing a high-pressure xenon gas TPC, AXEL (A Xenon ElectroLuminescence) for $0\nu\beta\beta$ decay searches. A unique feature of AXEL is its cellular readout scheme that also utilizes EL, called the electroluminescence light collection cell (ELCC). By using the ELCC, the AXEL detector has the potential for both high energy resolution and scalability. The concept and a proof-of-principle of the ELCC are described in Ref. [12]. In this paper, we describe the design of a larger prototype with a 180 L volume and evaluate its performance.

2. Detector design and construction

The final goal of the 180 L size prototype is to evaluate the detector performance in the energy region around the ^{136}Xe double-beta decay Q-value, 2458 keV. The detector components are housed in a vessel made of stainless steel (SUS304L) whose inner diameter is 547 mm, outer diameter 559 mm, and length 610 mm, for a total volume of 180 L. The vessel can withstand up to 10 bar of pressure. For the first phase of the 180 L prototype detector, we have constructed a small TPC with a sensitive region of 15 cm diameter and 10 cm length, as shown in Fig. 1. The primary purpose of the first phase is an evaluation of the performance and validation of the design of the detector components, with 511 keV gamma-rays. Ionization electrons are drifted to and detected by the ELCC (described in the next section) at the anode to measure the energy and topology of events in the volume. Scintillation light is detected by photomultiplier tubes (PMTs, R8520 Hamamatsu) at the cathode to determine the event timing.

2.1. *Electroluminescence light collection cell*

The ELCC is a detector to read out ionization electron signals in the AXEL TPC [12]. Each cell is a pixel on an anode plane. Ionization electrons are drawn into cells and produce EL photons that are detected by a silicon photomultiplier (SiPM) photon detector in each cell. The EL process has fewer fluctuations than electron avalanche counterpart and it is therefore expected to have better

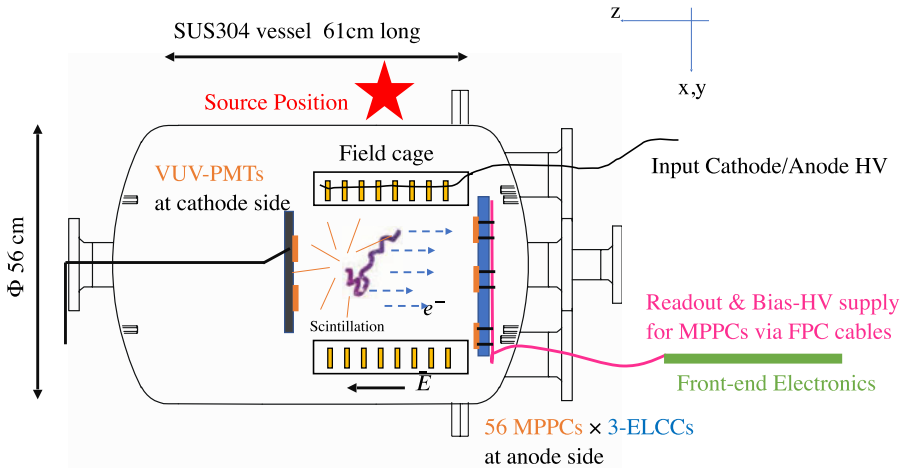

Fig. 1. Schematic view of the AXEL 180 L prototype chamber and a small field cage for the first-phase run. The source position is indicated by a red star.

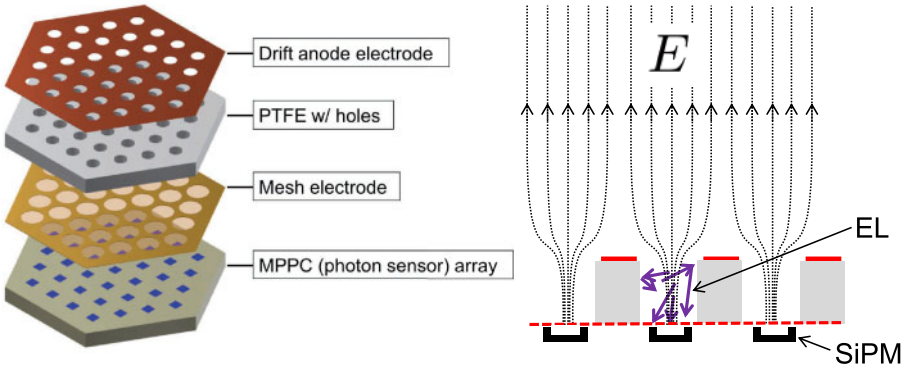

Fig. 2. Expanded (left) and cross-sectional (right) views of the concept of ELCC. The ELCC consists of four layers: drift anode electrode, PTFE plate, ground mesh electrode, and photon sensor array. Three top layers have patterned holes, and ionization electrons are drifted along the electric field into those cells. The EL photons are generated in the holes of the PTFE plate, between the anode electrode and the ground mesh electrode.

energy resolution than detectors based on the electron avalanche [13]. The pixel structure enables tracking. The ELCC plane consists of a drift anode electrode made of a 100 μm thick copper plate with holes, a 5 mm thick polytetrafluoroethylene (PTFE) plate with holes, a ground potential (GND) mesh, and SiPMs as shown in Fig. 2. The Hamamatsu 3×3 mm^2 S13370 multi-pixel photon counter (MPPC), which is sensitive to the vacuum ultraviolet (VUV) EL produced in xenon, is used as the SiPM. By applying a high voltage between the anode electrode and the GND mesh, an electric field that collects electrons is formed. When the electric field exceeds the EL threshold, EL photons are generated. The number of generated photons is given by the empirical formula [14]

$$Y_{\mathrm{EL}}/p = 140\,E/p - 116, \tag{1}$$

where Y_{EL} is the photon yield for 1 cm electron drift, E/p is the reduced electric field in units of kV/cm/bar, and p is the gas pressure in bar.

The dimension of the ELCC structure was optimized from the previous version [12]. In order to optimize the ELCC dimensions as follows, the energy resolution for 30 keV electrons was estimated for various configurations. The electric field is calculated by using gmsh [15,16] and Elmer [17]. Simulated electrons are generated 2 cm above the ELCC plane and tracked by Garfield++ [18]. Electroluminescence photons are generated based on the electric field along the electron track and Eq. (1) and the number of photons detected by the MPPC is calculated. The aperture ratio of the GND mesh (50%), photon detection efficiency of the MPPC (30%), distance between the GND mesh and MPPC (1 mm), and PTFE reflectivity (66% [19]) are taken into account. The ELCC response is obtained from this procedure. Next, 30 keV electrons are generated in the detector volume using Geant4 [20] and ionization electrons are generated, while taking the W-value and Fano factor into account. The position and time 2 cm above the ELCC plane after the drift are calculated based on diffusion constants estimated by MAGBOLTZ [21]. The number of detected photons for the 30 keV electron events is obtained using the ELCC response from above. The optimization is done at 30 keV because xenon has characteristic X-rays of that energy, making it straightforward to compare with data. The range of a 30 keV electron is 0.64 mm and its diffusion over a 10 cm drift is 3 mm in xenon at 8 bar. They are smaller than the typical ELCC cell pitch and enable sensitivity to EL-yield non-uniformity within the ELCC cell. The required energy resolution of 30 keV is 4.5% FWHM or less, to achieve 0.5% FWHM in terms of Q-value.

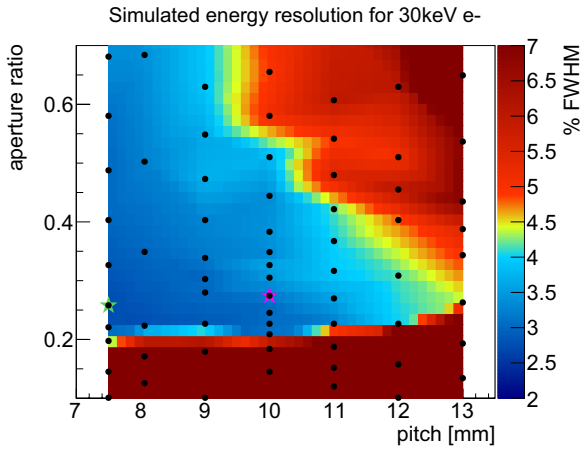

Fig. 3. Expected energy resolution for 30 keV electrons in xenon gas at 8 bar for various dimensions of the ELCC plane. Black dots represent simulation points. The color histogram is drawn by interpolation between the simulation points. The best parameters are found to be 7.5 mm for the pitch and 4 mm for the hole diameter and are shown by the green star. The adopted values, 10 mm for the cell pitch and 5.5 mm for the hole diameter, are shown by the magenta star.

Table 1. Expected number of detected photons and energy resolution for 30 keV electrons with optimized dimensions: 10 mm pitch, 5.5 mm hole diameter, and 5 mm thick EL region.

Pressure	Number of photons	Energy resolution (FWHM)
4 bar	9100	3.4%
8 bar	18 000	3.2%

The factors considered for the optimization are the cell pitch l_{pitch} and hole diameter d_{hole}. The EL field strength and the thickness of the PTFE plate are fixed at 3 kV/cm/bar and 5 mm, respectively. These numbers have been determined to give sufficient EL gain without necessitating excessive high voltage. Cells are aligned in a hexagonal pattern since the distance between them is shorter than the square pattern for the same aperture ratio as shown in Fig. 2.

Figure 3 shows the expected energy resolution for 30 keV electrons in xenon gas at 8 bar for various cell pitches and anode aperture ratios. If the aperture ratio is 0.2 or less, the electron collection efficiency is poor, and the energy resolution deteriorates significantly. For aperture ratios larger than 0.2, the smaller pitch and smaller aperture ratio give better energy resolution. For tracking purposes, a cell pitch of 10 mm is sufficient because the typical diffusion of electrons for a 1 m drift is 1 cm. A finer pitch increases the number of readout channels. From Fig. 3, a 10 mm pitch has 4.5% energy resolution, which is our requirement at 30 keV. The hole diameter that minimizes the energy resolution is 5 mm, but 5.5 mm was adopted in consideration of machining accuracy. Table 1 summarizes the expected number of detected photons and energy resolution. Since the measurement in this paper was performed at 4 bar, values at 4 bar are shown as well.

Following the result of the optimization, we constructed the ELCC with 10 mm pitch, 5.5 mm diameter anode electrode holes, a hexagonal cell pattern, and a 5 mm thick EL region. Figure 4 shows the ELCC plane installed as the first-phase 180 L prototype. The ELCC plane of this first-phase detector consists of three units. It is extendable to a larger size by adding units. Each ELCC unit has a trapezoidal shape and consists of a base plate made of polyetheretherketone (PEEK),

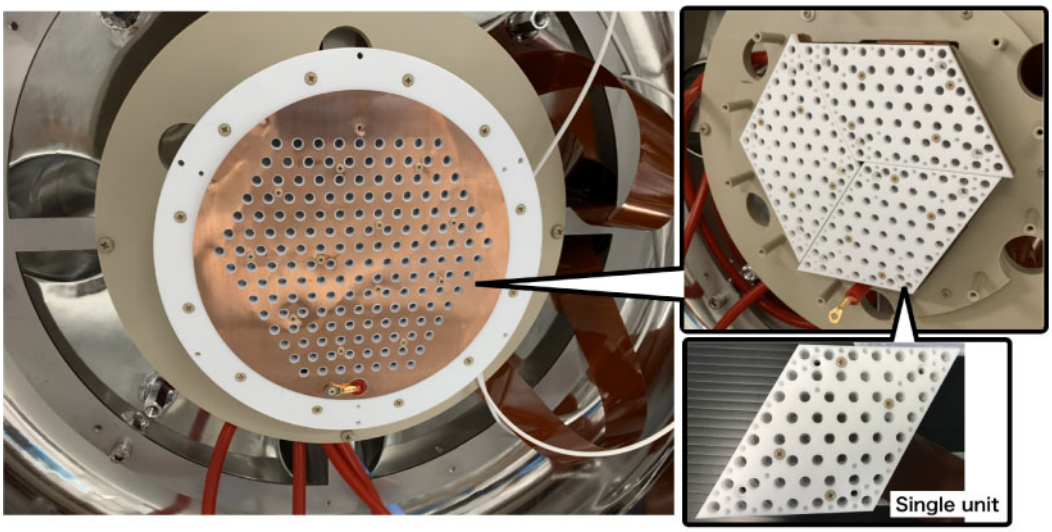

Fig. 4. Photograph of the ELCC in the first phase of the 180 L prototype detector. The left picture shows the full ELCC including the anode electrode. The top right picture shows three ELCC units without the anode electrode. The bottom right picture shows a single unit of the ELCC.

MPPCs on the base, a PTFE body with cells, an anode electrode, ground electrode, and a flexible printed circuit (FPC) on which MPPC signal and bias lines are printed (see Sect. 2.3). A single unit has 7×8 channels. The total number of channels is 168. The outermost 42 channels are set as veto channels and the remaining inner channels are regarded as fiducial channels. The anode electrode is a single plate made of oxygen-free copper. Tungsten mesh, with a wire diameter of 0.03 mm and an aperture ratio of 78%, is used as the GND mesh.

2.2. Drift electric field and field cage

To achieve high energy resolution, recombination between electrons and xenon ions should be suppressed because it reduces the number of initial ionization electrons and causes fluctuation in the signal size. The rate of recombination is suppressed with a large drift field. The large drift field is also preferred as it yields higher drift velocities and reduced diffusion. In contrast, the efficiency of collecting ionization electrons into the ELCC decreases if the ratio of the intensity of the drift field to the EL field is not sufficiently low. Hence we adopted a drift field of 100 V/cm/bar, which is acceptable for an EL field of 3 kV/cm/bar. Non-uniformity of the drift field causes non-uniformity of the recombination rate. Thus the drift field should be uniform to achieve high energy resolution. Based on the results of previous studies on the relation between recombination and electric field [22,23], we chose a target uniformity of $\pm 5\%$ for the intensity of the drift field. Note that these previous studies were conducted with alpha particles from ^{222}Rn in Ref. [22] and ^{241}Am in Ref. [23]. The rate of recombination for ionization by alpha particles is higher than that for ionization by electrons. Therefore this target value for uniformity is conservative.

The drift field is formed by a field cage that consists of a cathode mesh electrode on the PMT side, an anode electrode corresponding to the top electrode of ELCC, and ring electrodes aligned between the cathode and the anode. The ring electrodes are band-shaped copper strips with two different radii, one radius for inner and one for outer strips. A small overlap between the inner strips and the outer strips shields the effect of the vessel wall and maintains the uniformity of the drift field over

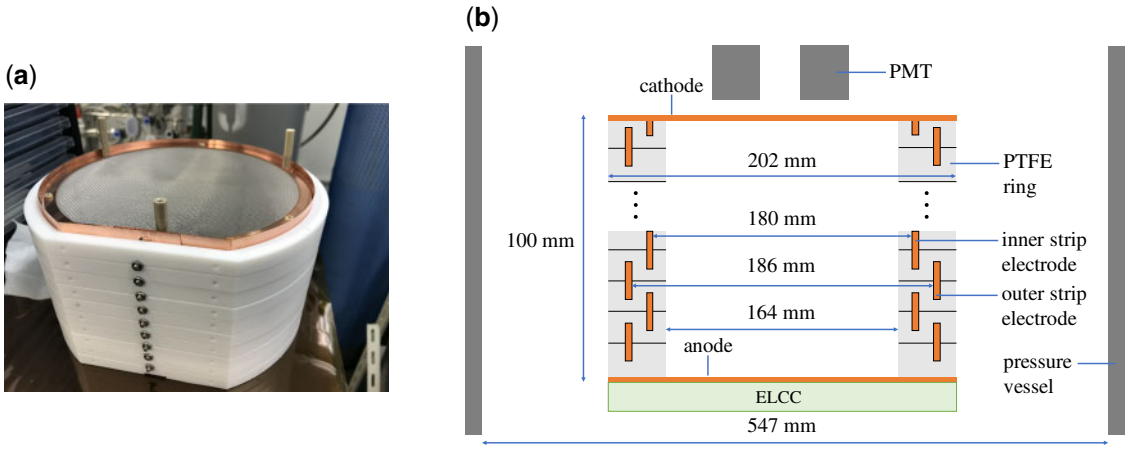

Fig. 5. Field cage for the first phase of the 180 L prototype. The left is a photograph and the right is the schematic cross-sectional view.

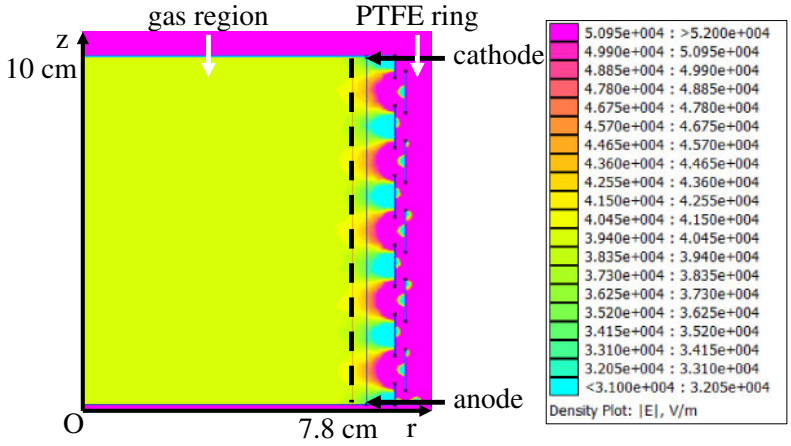

Fig. 6. Field intensity plotted on the field cage geometry. The field intensity deviates from 100 V/cm/bar by $\pm$ 5% where $r > 7.8$ cm.

a large volume inside the field cage. The electrodes are supported by PTFE rings, which also act as reflectors of VUV scintillation light to increase detection efficiency by the PMTs.

Figure 5a is a photograph of the field cage. The thickness and the width of the strips are 0.3 mm and 12 mm, respectively. Five inner electrodes and five outer electrodes are arranged at 10 mm intervals with 2 mm overlaps, resulting in a total drift length of 10 cm. The cathode electrode is a stainless steel mesh. The wire diameter of the cathode mesh is ϕ0.2 mm, and the wire is woven at an interval of 20 wires per one inch. Thus the aperture ratio of the cathode mesh is 71%. The mesh used for the first-phase prototype has a deflection, which changes the drift length. This deflection is roughly estimated to be within $\pm$1 cm. The anode electrode and the strip electrodes are connected in series by ten 100 MΩ resistors and the last inner electrode is connected directly to the cathode electrode. Detailed dimensions are shown in Fig. 5b.

Figure 6 depicts the electric field intensity calculated with FEMM [24]. The voltages were set to the values used in the measurement, -6.0 kV for the anode (V_{anode}), -10.0 kV for the cathode (V_{cathode}), and 0 V for the pressure vessel. These values correspond to a 3 kV/cm/bar EL field and a 100 V/cm/bar drift field for xenon gas at 4.0 bar. The result of the calculation shows that the

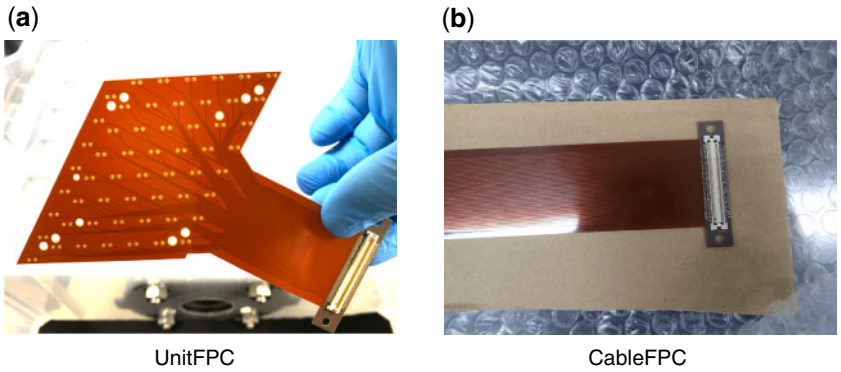

Fig. 7. FPCs for signal readout and application of bias voltage.

requirement of 100 V/cm/bar ± 5% is satisfied up to 4 mm inside the field cage ($r \leq 7.8$ cm) and covers the entire ELCC area.

2.3. Signal readout

At the bottom of the ELCC unit 56 MPPCs are mounted on another circuit FPC (unit FPC, see Fig. 7a) with connector pins. The lengths of the bias and signal lines on the unit FPC are slightly different among the MPPCs, but the timing differences are negligibly small compared to the timescale of EL light emission.

In order to connect an ELCC unit with a front-end electronics board (FEB) through the 83.1 mm diameter feedthrough of the chamber, we chose a double-sided FPC-based cable, a picture of which is shown in Fig. 7b. Twelve cable FPCs are mounted collectively on a feedthrough flange with epoxy molding. One FPC cable mounts 56 MPPC signal lines on the top side, 56 bias voltage lines on the bottom side, and four ground lines: 116 lines in total. The FPC cable is 30 mm in width and 500 mm in length and consists of a coverlay (50 μm), an adhesive (35 μm), a copper trace (33 μm), an adhesive (20 μm), a base polyimide (25 μm), an adhesive (20 μm), a copper trace (33 μm), an adhesive (35 μm), and a coverlay (50 μm). To suppress the cross-talk from neighboring lines, the signal and bias lines are designed to be 0.1 mm in width and 0.5 mm in pitch. The basic design of this FPC was developed by the NEXT Collaboration [6]. The unit FPC, the FPC cables, and the FEB are connected with FX11-LA connectors from Hirose Electric.

We developed a dedicated FEB that has two types of ADCs for different amplifier gain to achieve a wide dynamic range from 1 photon to $\sim 10^4$ photons/μs. One 40 MS/s, 2 V_{pp}, 12 bit ADC is connected to a higher-gain amplifier for every eight MPPCs via a multiplexer and is used for MPPC gain calibration. The other, a 5 MHz ADC connected to a lower-gain amplifier, is used for physics data taking. The effective gain of this FEB is 0.2 pC per ADC count. One FEB has 56 readout channels and acquires a waveform for up to 600 μs. This FEB also provides bias voltage to the MPPCs. The voltage is adjustable for each MPPC. Data are transferred to a DAQ PC via SiTCP Ethernet [25]. The details of the FEB are described in Ref. [26].

2.4. Gas system

A diagram of the xenon gas system is shown in Fig. 8. It is equipped with a vacuum pump system, a circulation compressor (MB-601HPAL, IBS), purification systems, gas analyzers, gas storage, and the AXEL prototype detector. Gas lines and the pressure vessel can store up to 10 bar of gas. Before filling the detector, the vessel is purged with argon gas and exhausted to 10^{-2} Pa to reduce

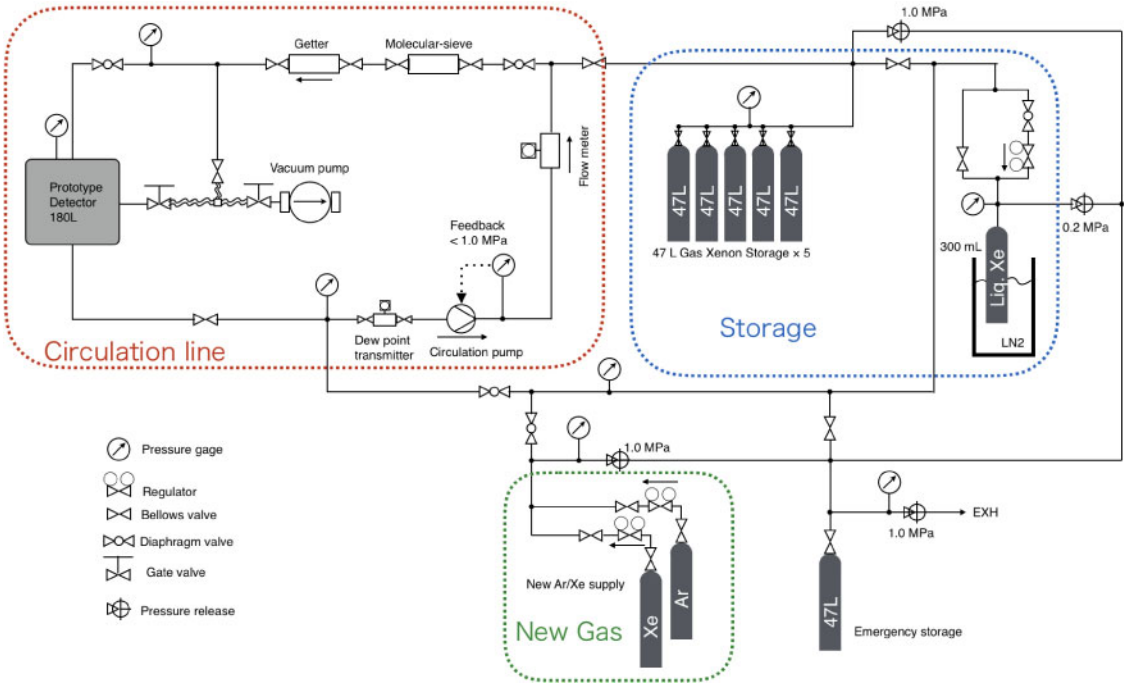

Fig. 8. Schematic view of the gas system.

outgassing from the detector using a scroll pump (ISP-250C, Anest Iwata) and a turbo-molecular pump (TG350FCAB, Osaka Vacuum). The rate of outgassing was $\sim 8.0 \times 10^{-5}$ Pa·m^3·s^{-1}. The xenon gas can be stored in five 47 L cylinders in the gaseous phase and in a 300 mL bin as liquid while the detector is opened. The system can hold a total of 2100 normal liters of xenon gas.

For the measurement below, we used about 4 bar of natural xenon gas with less than 100 ppm of contaminants. The gas is circulated during the data taking and a molecular sieve (MC1-902FV, SAES) and a nitrogen getter (API-GETTER-I-RE, API) maintain the purity of the xenon gas. A dew point transmitter (Pura, Michell Instruments) monitors the water concentration. Pressure gauges (ZT67, Nagano Keiki) measure the pressure with a precision of ±0.6 bar and monitor with much better resolution.

3. Measurement

The detector performance was evaluated by irradiating it with 511 keV annihilation gamma-rays from a ^{22}Na source. As a first long-term operation, we conducted this measurement at 4.0 bar, at which the high voltages are lower and commissioning is easier compared to the goal pressure of 8.0 bar. It also enables a comparison with the previous measurement with the smaller prototype [12]. The intensity of the ^{22}Na source was 7×10^5 Bq and was set outside the vessel (see Fig. 1). Data were taken for four days in December 2019. Figure 9 shows the various monitor data trends during the data taking. The electric fields in the EL and drift regions were set to 3.0 kV/cm/bar and 100 V/cm/bar, respectively. Although discharges happened mostly between the GND mesh and the anode electrode of the ELCC once per 6 hours on, shown as spikes in the figure, an interlock system cut and reset high voltage immediately. Xenon gas was circulated at 10 L/min and purified by the molecular sieve and the getter was operated at 400°C. The xenon gas pressure was stable at 4.0 ± 0.6 bar. The water concentration was slightly modified by the purification but its variation was smaller than the

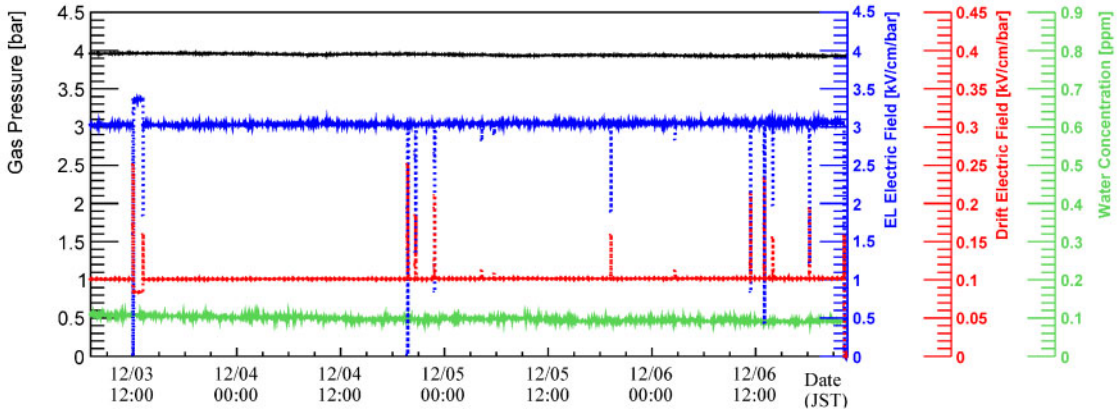

Fig. 9. Monitor values during the data taking. The black line shows the gas pressure in the prototype detector, the blue line is EL electric field, the red line is drift electric field, and the green line is the water concentration. Note that no calibration was applied for these data so the absolute values have non-negligible systematic error of the pressure gauges and the dew point transmitter. Spikes in the electric field values are due to anode-voltage discharges and trips.

systematic error of the dew point transmitter: 0.1 ± 0.1 ppm. Except for the discharges, the detector was stable for the entire data taking period.

The trigger was designed to issue when the height of the waveform sum of the inner channels exceeds a threshold and veto channels have no hits. However, due to a bug in the firmware, there were a few channel misidentifications between fiducial channels and veto channels. Complete veto was applied in the analysis stage, instead. In order to acquire 511 keV events efficiently, the threshold value was set high, roughly corresponding to 130 keV. A low-threshold trigger was set to acquire K_α (29.78 keV) events to calibrate the EL gain of each channel, as described in Sect. 4.2. The low-threshold trigger is reduced to 1/100 in order not to dominate the trigger rate. Coincidence of two PMTs that are mounted on the cathode side is required in order to prevent contamination of accidental backgrounds.

In total, 8100 166 events were acquired. Of these, 1000 000 events were used as a sample data set to determine the fiducial cut criteria and to establish the correction methods described below. The detector performance was evaluated using the entire data set.

4. Analysis

Typical signal waveforms of ELCC and PMTs are shown in Fig. 10. Two PMTs at the cathode detect the xenon scintillation signal and, 5–100 μs after that, EL signals are detected by the ELCC. The number of detected photons (photon counts) in each channel is obtained by integrating the waveform of each hit channel from the signal time of the signal's rise to its fall and dividing it by the gain of the channel's MPPC. The MPPC gains are measured using dark current pulses as described in Ref. [12]. For each hit channel, the non-linearity of the MPPC is corrected (Sect. 4.1) and the EL gain is calibrated (Sect. 4.2). The total number of photons in a given event is calculated by summing up the photon counts of all hit channels. The timing of the signal rise and fall of the event (T_{EL1} and T_{EL2}) are defined as the earliest rise time and the latest fall time among the hit channels (see Fig. 10). The photon counts are then converted to deposited energy (see Sect. 4.7). The hit position along the drift direction (z-position) is reconstructed from the time interval between the PMT signal (T_{scinti}) and the hit timing of the EL signal.

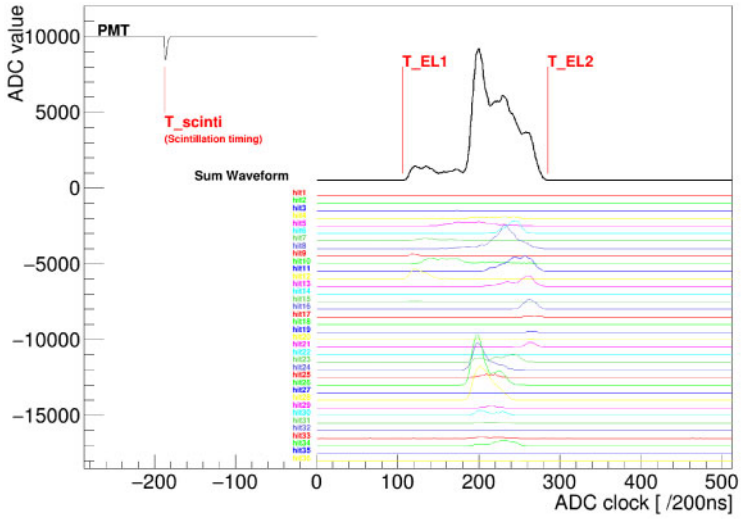

Fig. 10. Typical waveform and definition of parameters. The sum waveform is the waveform sum of the ELCC hit channels drawn as a colored waveform.

The detector performance was evaluated using photo-peaks at 511 keV (annihilation gamma-ray from ^{22}Na), 29.78 keV (characteristic K_α X-ray), and 33.62 keV (characteristic K_β X-ray). To obtain clear photo-peaks, fully contained events in the fiducial region are selected (Sect. 4.3). Additional corrections and cuts are described in Sects. 4.4–4.6.

4.1. MPPC non-linearity correction

The linearity of the MPPCs degrades when the number of irradiated photons is comparable to the number of APD pixels constituting the MPPC. This is because each APD pixel is operated in Geiger mode and is not able to distinguish multiple photons. Based on simulation, the maximum number of photons detected by a single MPPC is expected to reach $\sim 10^4$ photons in a few tens of μs for $0\nu\beta\beta$ signals. Although 10^4 is much more than the number of pixels of the S13370 MPPC, $N_{\mathrm{pixel}} = 3600$, since the photons are distributed over tens of μs and the signal does not fully saturate and can be corrected. The correction is performed with the following function:

$$N_{\mathrm{observed}} = \frac{N'_{\mathrm{observed}}}{1 - \tau \cdot N'_{\mathrm{observed}}/(N_{\mathrm{pixel}} \cdot \Delta t)}, \tag{2}$$

where N'_{observed} is the number of observed photons before correction and Δt is set to 200 ns, which corresponds to the sampling time of the 5 MS/s ADC. This equation is derived in A. Here τ is the MPPC pixel recovery time and was found to be around 120 ns according to our linearity measurement of MPPC. In this analysis, the same value is used for all MPPCs, 120 ns, as it gives the best energy resolution for the characteristic X-ray peaks ($\sim$ 30 keV) for the sample data set.

4.2. EL gain calibration

Electroluminescence gain (EL gain) is defined as the average number of EL photons detected when one ionization electron enters a cell and is estimated for each cell using the photon counts of the K_α peak. For each channel, events are chosen in which that channel observed the largest number of photons, and there are no other hits except for the two layers of surrounding channels (see Fig. 11).

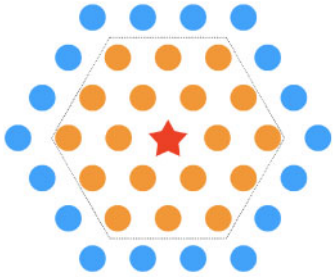

Fig. 11. Selection of events for the EL gain calibration. The center channel represented by the red star is the channel being calibrated. That channel has to have the largest number of photons. All other channels except for the two layers of surrounding channels represented by orange circles are required not to have hits.

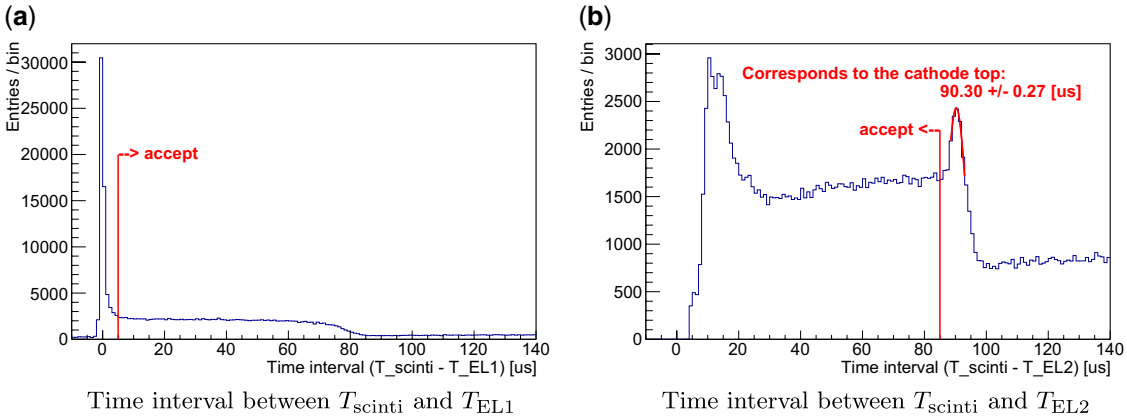

Time interval between T_{scinti} and T_{EL1} Time interval between T_{scinti} and T_{EL2}

Fig. 12. Distributions of time interval between the scintillation signal and EL signal.

The EL gain at 29.78 keV is obtained as the central value of the K_α peak after fitting with a Gaussian.

Throughout this process the gains of the surrounding channels affect the calibration and therefore the calibration has to be iterated multiple times. In this analysis, the EL gain calibration was repeated five times for all channels and an additional four times for the fiducial channels.

4.3. Fiducial volume cut

Events that only have hits in the fiducial channels of the ELCC plane are selected.

Figure 12 shows the distributions of the interval between T_{scinti} and T_{EL1} (Fig. 12a) and between T_{scinti} and T_{EL2} (Fig. 12b) of the sample data set after the fiducial channel cut. The peak structure in Fig. 12 corresponds to events that hit the anode electrode. The right peak in Fig. 12b corresponds to the events that crossed the cathode electrode. To chose fully contained events along the drift direction, events whose time interval $T_{\mathrm{scinti}} - T_{\mathrm{EL1}}$ is more than 5.0 μs and time interval $T_{\mathrm{scinti}} - T_{\mathrm{EL2}}$ is less than 85 μs are selected. The flat distribution above 100 μs in Fig. 12b is due to contamination of accidental hits and EL signals. The contamination is high because the current PMT readout electronics has only timing information without waveform or pulse height.

Since the cathode is at $z = 10 \pm 1$ cm the drift velocity of electrons in the detector can be measured by comparing the timing of events crossing the cathode with those at the anode ($z = 0$ cm). The error of the cathode position comes from the distortion of the stainless mesh electrode as mentioned in Sect. 2.2. Fitting the cathode timing in Fig. 12b with a Gaussian yields 90.30 ± 0.27 μs and thus the

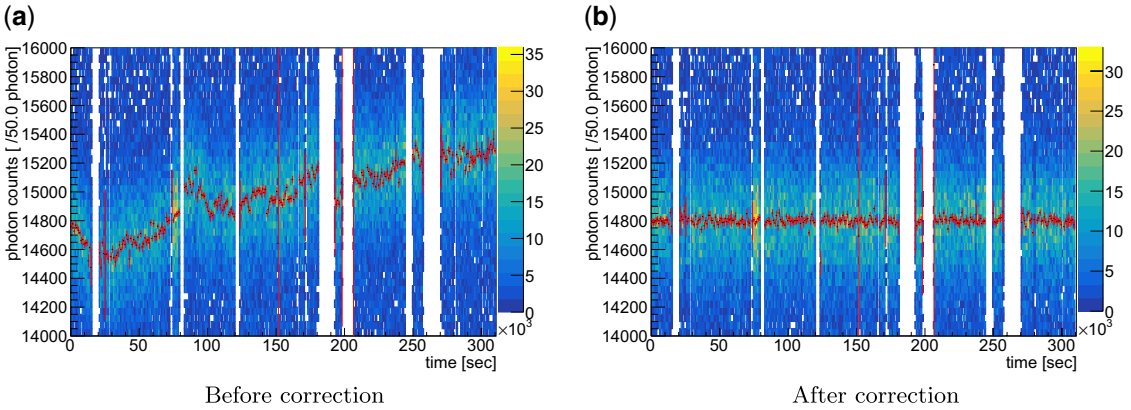

Fig. 13. Variation of light yield as a function of time before (a) and after (b) the correction. Black dots and red lines represent the K_α peak position and its fitting error in each time bin, respectively. Empty bins are run changes or periods of DAQ troubles.

drift velocity is 0.11 ± 0.01 cm/μs. This value is comparable to a previous study [27]. The 1σ peak width estimated from this fit is 4.54 μs and corresponds to 0.50 cm at the drift velocity of 0.11 cm/μs. This spread of the peak is caused by diffusion during drift and means that the reconstructed z-position has at most a 0.5 cm uncertainty.

4.4. Time dependence correction

Figure 13a shows the time dependence of the light yield. The change in the light yield is possibly caused by an improvement of gas purity and change in the gas density. The data acquisition period is divided into 300 bins, and correction for the time dependence of the K_α peak to be flat is applied (Fig. 13b).

4.5. Correction for z-dependence

Figure 14 shows the photon counts of the K_α peak as a function of the z-position defined as the weighted average of the light amount. The light yield decreases for events far from the ELCC. This is considered to be due to loss of ionization electrons due to capture by impurities such as oxygen. In the region below 3 cm, the light yield increases non-linearly. Non-uniformity of the light yield depending on the event position relative to the cell position is also observed in that region. The position dependence on the initial electron position 2 cm above the ELCC is also reproduced by a simulation at 4 bar.

The reduced yield in 3 cm$\leq z \leq$10 cm is fitted with a linear function. Using the fitted parameters, the z-dependence is corrected to be flat for every sampling point of the 5 MS/s ADC.

4.6. Additional z cut

As mentioned in Sect. 4.5, non-uniformity depending on the position relative to the cell position is remnant at $z < 3$ cm. Therefore, events whose z-position at the time of their signal's rise is less than 3.5 cm are cut.

4.7. Result of cuts and corrections

The change in the energy spectrum after each fiducial volume cut is shown for the sample data set in Fig. 15. Figure 16 shows the change in the energy spectrum after all corrections and the additional z

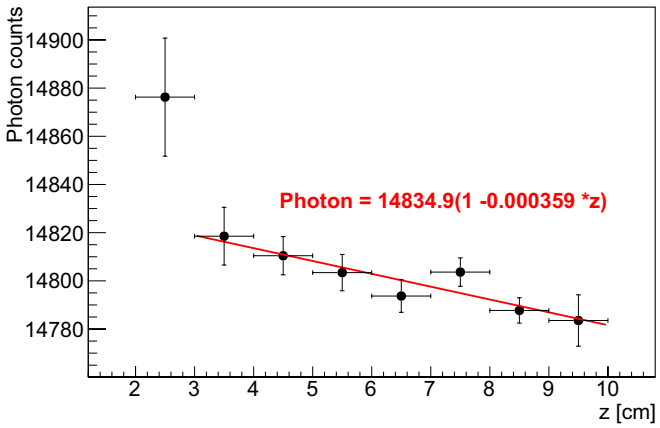

Fig. 14. z-dependence of light yield for the K_α peak.

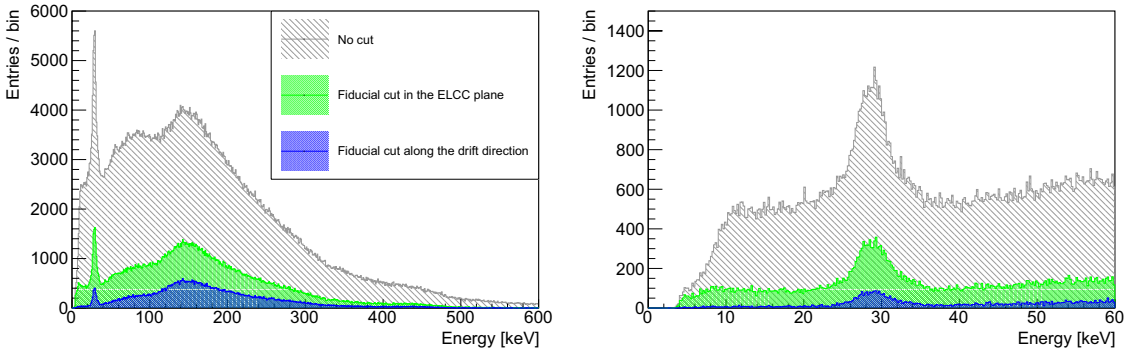

Fig. 15. Change in the energy spectrum after cuts for the sample data set. The right figure shows only the region around 30 keV.

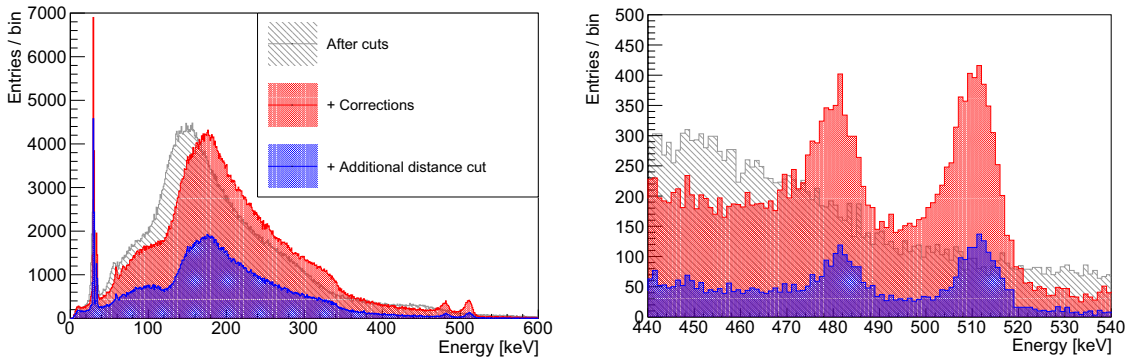

Fig. 16. Change in the energy spectrum by corrections and the additional distance cut for the whole data set. The right figure is an enlargement around 511 keV.

cut for the whole data set. After these corrections and cuts, peak structures at 511 keV and ∼480 keV (escape peaks) are clearly seen. In these histograms, the energy scale is calibrated using the photon counts of two characteristic X-ray peaks (29.78 keV, 33.62 keV) and a 511 keV peak.

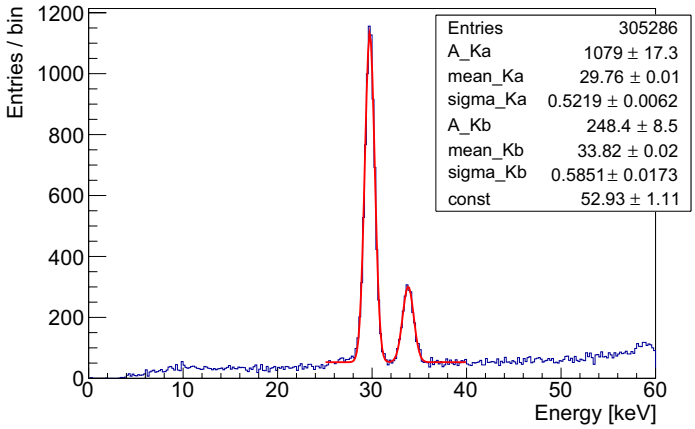

Fig. 17. Energy spectrum around 30 keV and fit result to two Gaussian functions and a constant.

5. Detector performance

5.1. *EL yield*

The total photon counts of K_α events and 511 keV events are 14 805 ± 3.08 and 256 773 ± 140.3, respectively. The expected number of photons of 30 keV events at 4 bar was 9100, as mentioned in Sect. 2.1. This inconsistency may be due to systematic error of MPPC detection efficiency, the reflectivity of PTFE, and the angular dependence of incident photons relative to the GND mesh.

5.2. *Electron lifetime*

The lifetime of electrons during drift is estimated from the z-dependence described in Sect. 4.5. The correction coefficient, $1 - az$, can be cast as

$$1 - az \simeq \exp(-az), \tag{3}$$

where a is the slope of the correction, 0.000 359 ± 0.000 120. This leads to a $1/e$ decay length of

$$1/(0.000\,359 \pm 0.000\,120) = 2785.51 \pm 931.09 \text{ cm}. \tag{4}$$

Conversion to the electron lifetime using the drift velocity, 0.11 ± 0.01 cm/μs, yields 25.32±8.77 ms.

5.3. *Energy resolution*

Figure 17 shows the energy spectrum around the characteristic X-rays of xenon and their fitting result with double-Gaussian plus constant. The obtained energy resolutions are 4.10 ± 0.05% (FWHM) and 4.06 ± 0.14% (FWHM) for the K_α and K_β peaks, respectively. Figure 18 shows the energy spectrum around 480 keV and 511 keV. The peak at around 480 keV consists of the escape peaks of K_α (481.22 keV) and K_β (477.38 keV). Accordingly, this peak was fitted using a double-Gaussian with the peak positions of the fitting function fixed to each characteristic energy. The 511 keV peak was fitted with a single Gaussian. A linear function was added to model the continuum components. The obtained energy resolution is 1.73 ± 0.07% (FWHM) for 511 keV, which corresponds to 0.79 ± 0.03% (FWHM) at the ^{136}Xe $0\nu\beta\beta$ decay Q-value when extrapolated by $\sqrt{E}$.

The resolution at the Q-value was also evaluated assuming an additional energy dependence term using the form $A\sqrt{E + BE^2}$, where A and B are the fitting parameters. The resolutions at the K_α, K_β, and 511 keV peaks are used in the evaluation with this function.

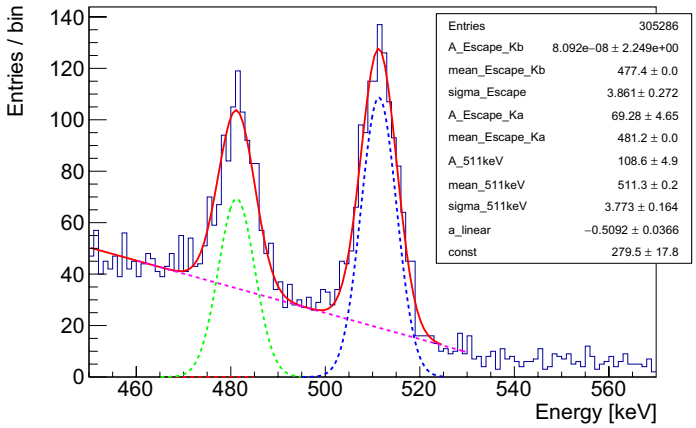

Fig. 18. Energy spectrum around 511 keV and fit result. The peak structure at 480 keV consists of the K_α and K_β escape peaks. The escape peaks are fitted with a double-Gaussian and 511 keV peak is fitted with a Gaussian. The continuum component is fitted with a linear function.

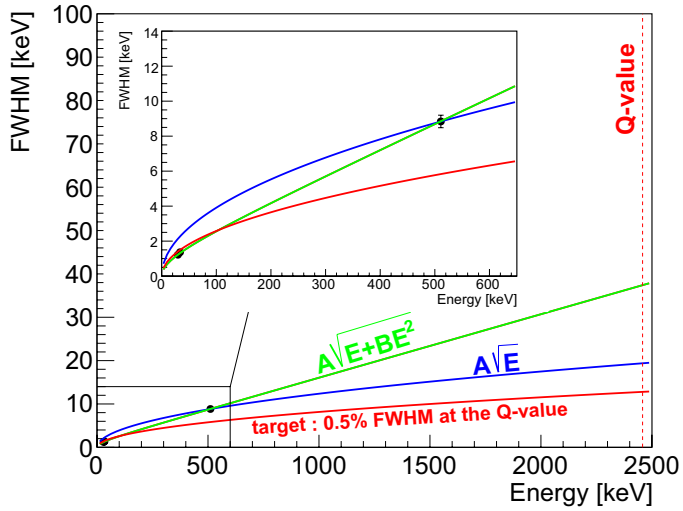

Fig. 19. Extrapolation to the Q-value of ^{136}Xe $0\nu\beta\beta$ decay with two types of function: $A\sqrt{E}$ and $A\sqrt{E+BE^2}$. The evaluation is performed with the resolution at 511 keV only for $A\sqrt{E}$ (blue curve) and with the resolutions at the K_α, K_β, and 511 keV peaks for $A\sqrt{E+BE^2}$ (green curve). The red curve represents our target energy resolution (0.5% FWHM at the Q-value).

Figure 19 shows the result. The extrapolated energy resolution (FWHM) at the Q-value, 2458 keV, is estimated to be 1.52% (FWHM). This value does not reach the target resolution, 0.5%, since the peak resolution at 511 keV is worse than the resolution of the characteristic X-ray peaks. The reason for this will be investigated by evaluating the expanded 180 L prototype using gamma-rays of higher energy in the future. It is possible that the sensitive area is restricted by the cut in Sect. 4.6, and events with a small spread in the z direction are collected selectively. Study with a larger fiducial volume is desired.

5.4. Event topology

Figure 20 shows an example event display of a 511 keV event. A blob structure at the track endpoint can be clearly seen. The number of blobs can be an index indicating the number of electron tracks. By determining the number of blobs, gamma-ray backgrounds and $0\nu\beta\beta$ signals can be distinguished.

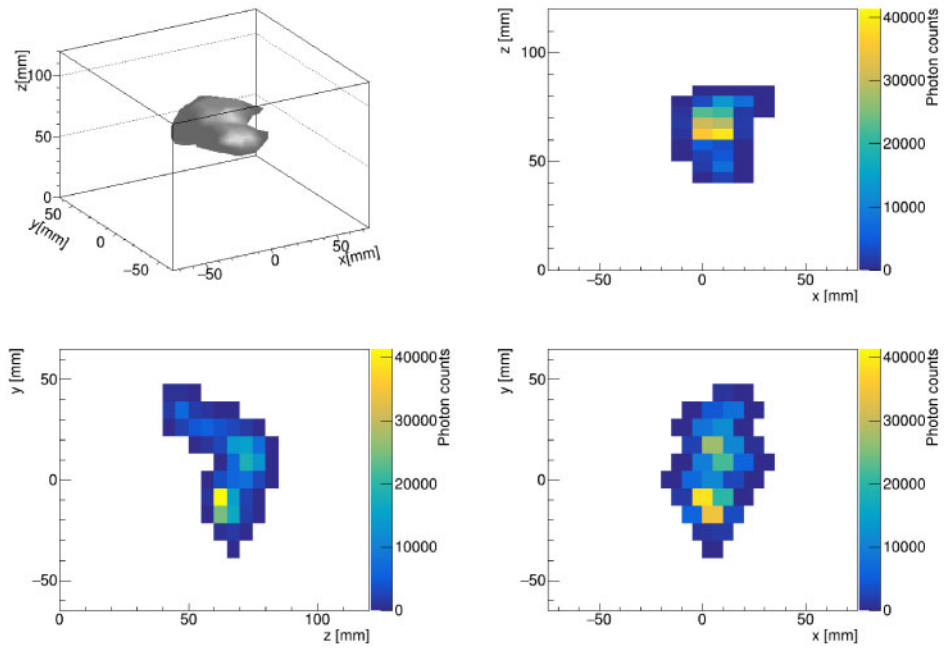

Fig. 20. Event display of an event with 511 keV of deposited energy. The z direction is sampled every 0.22 mm, but in this event display it is merged to 5 mm for easy viewing.

An eye scan shows that about half of the events have similar structures at their track endpoint. Five more event displays with the energy deposit of 511 keV are shown in B. Algorithms to distinguish $0\nu\beta\beta$ signals from gamma-ray backgrounds using topological information and the machine learning method have been actively studied in xenon gas TPC experiments for $0\nu\beta\beta$ decay searches [28,29]. We are also studying an algorithm based on DenseNet [30] for a future physics run [31].

6. Conclusion

AXEL is a high-pressure xenon gas TPC with a unique cellular readout scheme, ELCC, that is being designed to search for $0\nu\beta\beta$ decay. We developed a 180 L size prototype detector with excellent energy resolution and scalability. The dimension of the ELCC has been optimized using simulations to achieve an energy resolution of 0.5% at the ^{136}Xe $0\nu\beta\beta$ Q-value, 2458 keV. Commissioning data were taken at 4 bar with 511 keV gamma-rays from a ^{22}Na source and the obtained energy resolution is $1.73 \pm 0.07\%$ (FWHM). The energy resolution at 2458 keV was estimated to be $0.79 \pm 0.03\%$ (FWHM) based on extrapolation from only the 511 keV peak using an $A\sqrt{E}$ function. Combined with evaluations of the K_α and K_β peaks, the estimated energy resolution at the Q-value is 0.79–1.52% (FWHM). Ionization electron tracks are reconstructed from the hit patterns and hit timings in the ELCC. The structure at the endpoint of the electron track (blob) can be seen in this track information. Measurement at a higher energy will be performed with the upgraded next-phase detector and at higher pressure to further improve the energy resolution and demonstrate the performance at the $0\nu\beta\beta$ Q-value.

Acknowledgements

The AXEL experiment is supported by the Japan Society for the Promotion of Science (JSPS) KAKENHI Grant Numbers 15H02088, 16J09462, 17K18777, 17J00268, 18J13957, 18J00365, 18J20453, and 18H05540. We also thank the Institute for Cosmic Ray Research and Kamioka underground laboratory, the University

of Tokyo, for their support of our project. The development of the electronics board is supported by Open-It (Open Source Consortium of Instrumentation), High Energy Accelerator Research Organization (KEK). We thank R. Wendell for his help in preparing the manuscript.

Appendix A. MPPC recovery time

To model the relationship between the output signal of the MPPC and the number of incident photons, we consider N_{observed} photons incident on an MPPC during Δt seconds. Here, only photons that create an electron–hole pair in the MPPC sensitive region are considered. Using the amount of photons per unit time per MPPC pixel, $k \equiv N_{\text{observed}}/(\Delta t \cdot N_{\text{pixel}})$, where $N_{\text{pixel}} = 3600$ is the number of pixels on an S17330 MPPC and Δt is set to 200 ns corresponding to 1 clock of the ADC, the probability that a photon enters a particular MPPC pixel again t seconds after the pixel detects a preceding one can be expressed as ke^{kt}.

The recovery time τ is defined as the time required for the pixel gain to recover to $(1 - 1/e)$ times the original gain, g_0, after the pixel emits a pulse. Thus, a gain t seconds after the previous pulse is represented as $g_0(1 - e^{-t/\tau})$, and the average gain g is calculated as

$$g = \int_0^\infty ke^{kt} g_0 (1 - e^{-\frac{t}{\tau}}) dt = \frac{g_0}{1 + k\tau}. \tag{A.1}$$

The output by an MPPC with gain g is

$$N'_{\text{observed}} = \frac{N_{\text{observed}}}{1 + k\tau}. \tag{A.2}$$

Hence, solving for N_{observed}, the number of true incident photons can be estimated with the recovery time τ from the number of observed photons N'_{observed} as in Eq. (2).

Appendix B. Additional event display

Five example event displays with a deposited energy of 511 keV are shown in Figs. B.1–B.5. In these figures, data along the z direction are merged to 5 mm as described in Fig. 20.

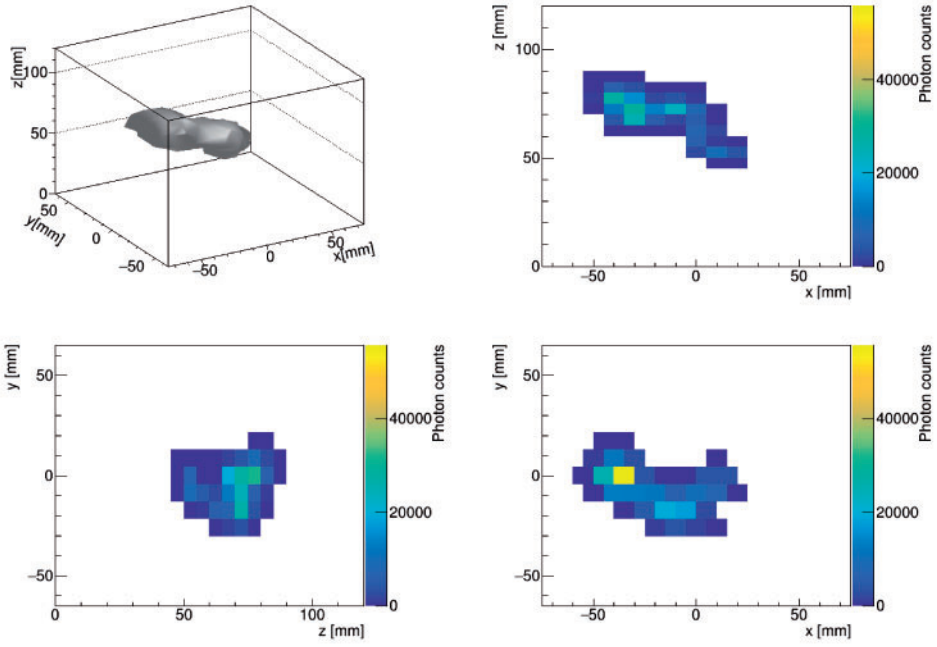

Fig. B.1. Event display of a 511 keV event.

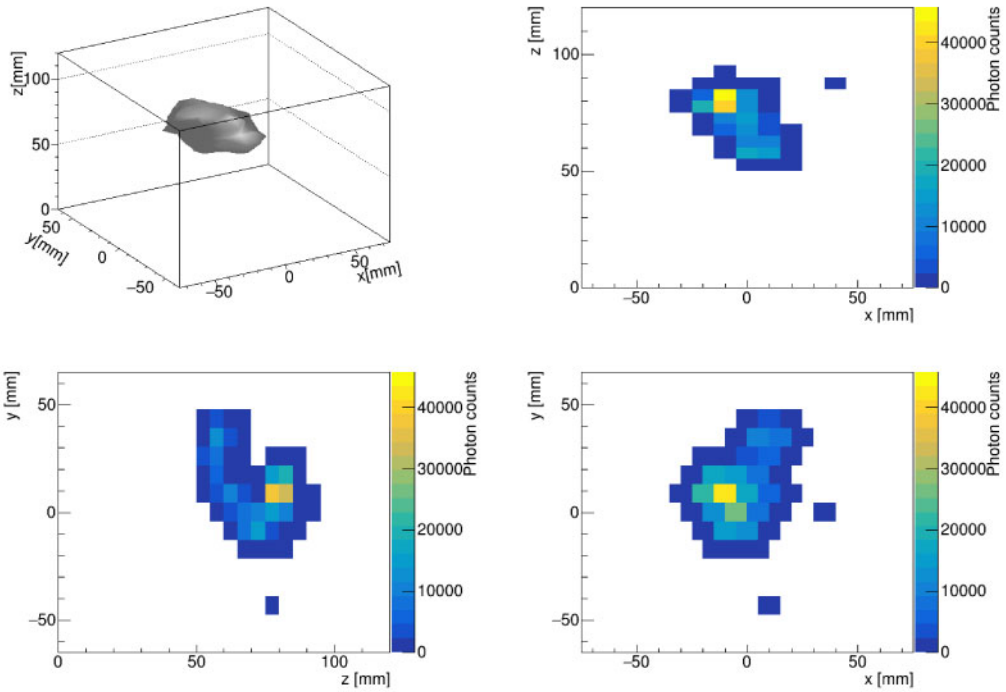

Fig. B.2. Event display of a 511 keV event.

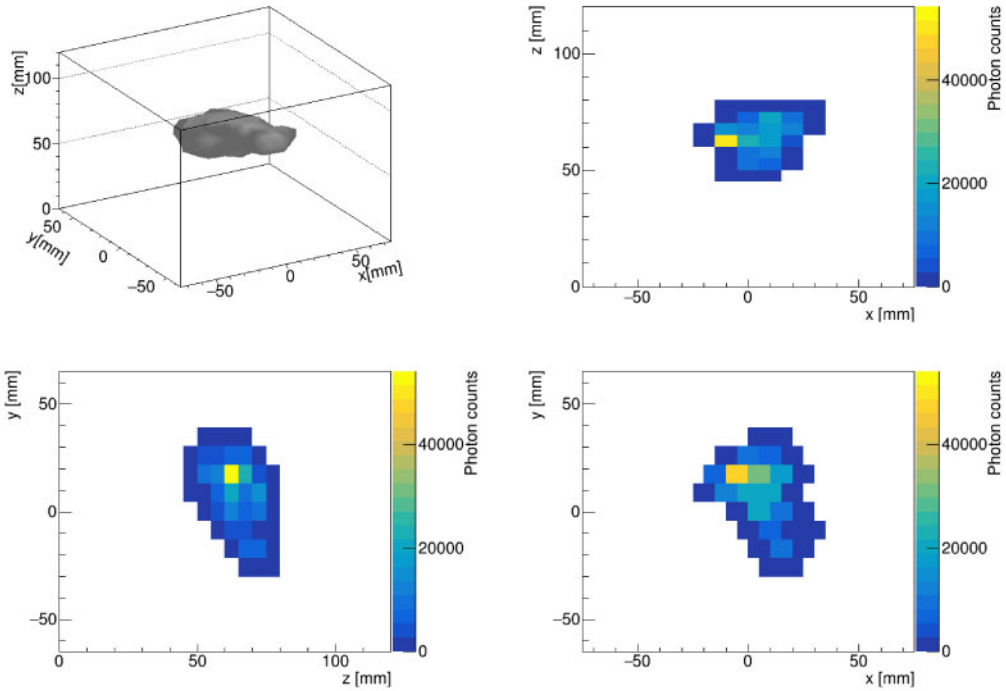

Fig. B.3. Event display of a 511 keV event.

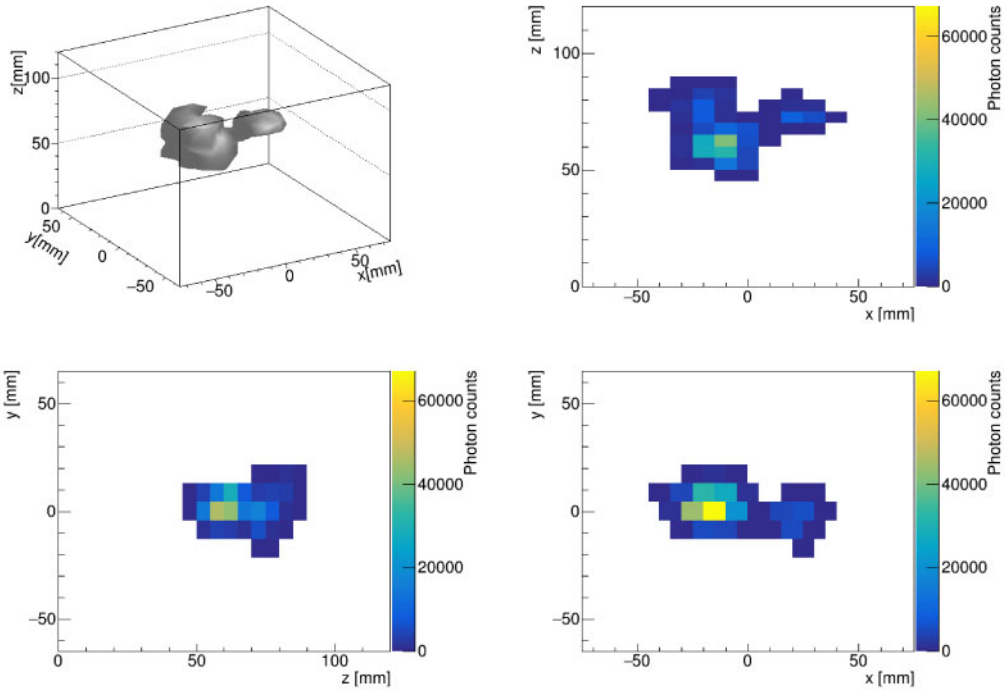

Fig. B.4. Event display of a 511 keV event.

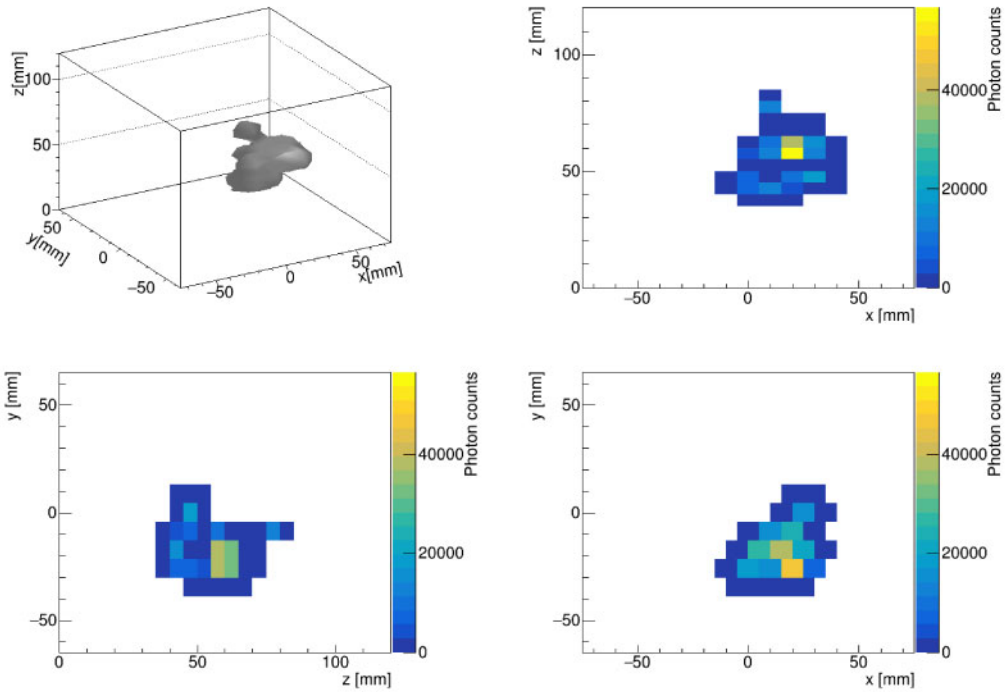

Fig. B.5. Event display of a 511 keV event.

References

[1] M. Fukugita and T. Yanagida, Phys. Lett. B **174**, 45 (1986).
[2] T. Yanagida, Horizontal gauge symmetry and masses of neutrinos, in *Proceedings: Workshop on the Unified Theories and the Baryon Number in the Universe*, eds. O. Sawada and A. Sugamoto (National Laboratory for High Energy Physics, Tsukuba, Japan), p. 99.
[3] M. Gell-Mann, P. Ramond, and R. Slansky, Complex Spinors and Unified Theories, in *Supergravity Workshop Stony Brook*, eds. P. van Niewwen-huizen and D. Z. Freedman (North Holland, Amsterdam, 1979), Vol. C790927, p. 315.
[4] A. Gando et al. [KamLAND-Zen Collaboration], Phys. Rev. Lett. **117**, 082503 (2016); 117, 109903 (2016) [erratum].
[5] D. R. Nygren, B. J. P. Jones, N. López-March, Y. Mei, F. Psihas and J. Renner J. Instrum. **13**, P03015 (2018).
[6] V. Álvarez et al., J. Instrum. **7**, T06001 (2012).
[7] X. Chen et al., Sci. China Phys. Mech. Astron. **60**, 061011 (2017).
[8] V. Álvarez et al., J. Instrum. **8**, P04002 (2013).
[9] V. Álvarez et al., J. Instrum. **8**, P09011 (2013).
[10] J. Renner et al., J. Instrum. **13**, P10020 (2018).
[11] S. Wang, Nucl. Instrum. Meth. Phys. Res. A **958**, 162439 (2020).
[12] S. Ban et al., Nucl. Instrum. Meth. Phys. Res. A **875**, 185 (2017).
[13] A. Bolotnikov and B. Ramsey, Nucl. Instrum. Meth. Phys. Res. A **396**, 360 (1997).
[14] C. M. B. Monteiro, L. M. P. Fernandes, J. A. M. Lopes, L. C. C. Coelho, J. F. C. A. Veloso, J. M. F. dos Santos, K. Giboni and E. Aprile, J. Instrum. **2**, P05001 (2007).
[15] C. Geuzaine and J.-F. Remacle, Int. J. Numer. Meth. Eng. **79**, 1309 (2009).
[16] C. Geuzaine and J.-F. Remacle, (2009) (available at: http://gmsh.info/, date last accessed 6 March 2020).
[17] M. Malinen and P. Raback, *Elmer* (available at: https://www.csc.fi/web/elmer/, date last accessed 6 March 2020).
[18] K. Baraka et al., *Garfield++ – simulation of tracking detectors* (available at: https://garfieldpp.web.cern.ch/garfieldpp/, date last accessed 6 March 2020).
[19] C. Silva, J. Pinto da Cunha, A. Pereira, V. Chepel, M. I. Lopes, V. Solovov, and F. Neves, J. Appl. Phys. **107**, 064902 (2010).
[20] S. Agostinelli et al., Nucl. Instrum. Meth. Phys. Res. A **506**, 250 (2003).
[21] S. Biagi, *Magboltz – transport of electrons in gas mixtures* (1995), (available at: http://magboltz.web.cern.ch/magboltz, date last accessed 6 March 2020).
[22] L. Serra et al., J. Instrum. **10**, P03025 (2015).
[23] K. D. Nakamura et al., J. Instrum. **13**, P07015 (2018).
[24] D. C. Meeker, *Finite element method magnetics*, version 4.2 (2018), (available at: https://www.femm.info/wiki/HomePage, date last accessed 6 March 2020).
[25] T. Uchida, IEEE Trans. Nucl. Sci. **55**, 1631 (2008).
[26] K. Z. Nakamura, S. Ban, A. K. Ichikawa, M. Ikeno, K. D. Nakamura, T. Nakaya, S. Obara, S. Tanaka, T. Uchida, M. Yoshida (AXEL collaboration), [arXiv:2001.02104 [physics.ins-det]] [Search INSPIRE].
[27] V. Álvarez et al., J. Instrum. **8**, P05025 (2013).
[28] J. Renner et al., J. Instrum. **12**, T01004 (2017).
[29] H. Qiao et al., Sci. China Phys. Mech. Astron. **61**, 101007 (2018).
[30] G. Huang et al., 2017 IEEE Conf. Computer Vision and Pattern Recognition (CVPR), p. 2261 (2017).
[31] S. Obara et al., Nucl. Instrum. Meth. Phys. Res. A **958**, 162803 (2020).